Multi-scale Designed $Co_xMn_{3-x}O_4$ Spinels: Smart Pre-Catalysts towards High-Efficiency Pyrolysis-Catalysis Recycling of Waste Plastics

Xingmin Liu[1,a], Dan Xu[2,a*], Hui Ding[1], Marc Widenmeyer[1], Wenjie Xie[1], Maximilian Mellin[1], Fangmu Qu[1], Guoxing Chen[3], Ye Shui Zhang[2,4], Zhenyu Zhang[2], Aasir Rashid[1], Leopoldo Molina-Luna[1], Jan P. Hofmann[1], Ralf Riedel[1], Dan J. L. Brett[2], Anke Weidenkaff[1,3 *]

[1] Institute of Materials Science, Technische Universität Darmstadt, Alarich-Weiss-Str. 2, 64287, Darmstadt, Germany

[2] Electrochemical Innovation Lab, Department of Chemical Engineering, University College London, London WC1E 7JE, UK

[3] Fraunhofer Research Institution for Materials Recycling and Resource Strategies IWKS, Brentanostraße 2a, 63755 Alzenau, Germany

[4] School of Engineering, University of Aberdeen, Aberdeen, AB24 3UE, UK

[a] These two authors make equal contribution to this work.

[*] Corresponding authors: danxu_joey@163.com (D. Xu); anke.weidenkaff@mr.tu-darmstadt.de or anke.weidenkaff@iwks.fraunhofer.de (A. Weidenkaff)

Highlights

• Multiscale designed $Co_xMn_{3-x}O_4$ spinel smart pre-catalysts that can self-convert into the targeted active site-rich Co/MnO catalysts are developed to recycle waste plastics.

• The physical mechanism of superior catalytic performance of Co/MnO is pinpointed via DFT calculation.

• The specific carbon nanotube composites and H_2 yield of the Co/MnO catalyst reach a new record high.

• The plastic converted carbon nanotube composites were tested to be excellent anode materials for lithium-ion batteries.

Abstract

In this work, multiscale designed 3-dimensional (3D) rose-like $Co_xMn_{3-x}O_4$ spinel smart pre-catalysts that can self-convert into the targeted active site-rich Co/MnO catalysts were developed for the high-efficiency conversion of waste plastics. At a pre-catalyst to plastic weight ratio of 1:14, the carbon nanotube composites (CNCs) and H_2 yield can reach 41 wt.% and 36 $mmol \cdot g^{-1}_{pla.}$, while the specific CNCs and H_2 yield can be as high as 7.48 $g^{-1}_{cat.}$ and 634 $mmol \cdot g^{-1}_{pla.} \cdot g^{-1}_{cat}$. The latter is more than one order of magnitude higher than reported in the literature. Density functional theory calculations indicate that the Co/MnO catalyst exhibits excellent activity in the dissociation of alkanes (e.g., CH_4). The resulting CNCs demonstrated excellent discharge capability and extended cycling performance when used as a lithium-ion battery anode. This work revealed an innovative recipe and novel insight for developing advanced catalyst materials as the next generation catalysts for the conversion of waste plastics.

Keywords: waste plastics; $Co_xMn_{3-x}O_4$ spinels; carbon nanotube composites; H_2 production; pyrolysis-catalysis

1. Introduction

As a response to the “zero polution” action plan and energy transition, considerable efforts have been made to develop clean and renewable energy conversion to replace the traditional energy systems (e.g., fossil fuels)[1-5]. Hydrogen (H_2), as a clean and reliable alternative to fossil fuels, has

been widely employed as a clean energy carrier in transport engines and fuel cells[4-6]. As an alternative, rechargeable lithium ion batteries (LIBs) with high energy density have also been found to be promising energy sources for portable electronics and electrical vehicles[7-11]. In this context, carbon nanotube composites (CNCs, e.g., carbon nanotubes (CNTs)@metal oxides) have shown convincing potential as anode materials in LIBs[9-12]. A common shortcoming is that by now methane is still the primary source for the production of H_2 through thermochemical conversion and the fabrication of CNCs[13,14]. In parallel, the rapid development of all walks of life has led to a substantial accumulation of plastic wastes, leading to disruptive environmental problems[13-15]. Simultaneous co-production of H_2 and CNCs via pyrolysis-catalysis offers an alternative and cost-effective feedstock for the large-scale production of H_2 and CNCs, and a sustainable way to recycle waste plastics[13,15].

Catalyst plays a critical role in enhancing the production of H_2 and CNCs[16,17]. Non-noble transition metals (e.g., Fe, Co, and Ni nanoparticles) are the most widely used catalysts due to their excellent catalytic activity, low cost, and high abundance [13-17]. For easy processibility, metal oxide pre-catalysts were employed for the pyrolysis-catalysis conversion, where the pre-catalysts were reduced in situ into metallic catalysts by the hydrocarbons derived from the decomposition of plastic wastes prior to the catalytic conversion[13,15]. Moreover, limited by the intrinsic properties of the catalysts, support materials (e.g., γ/α-Al_2O_3, SiO_2, and zeolites) have to be employed to prohibit sintering and agglomeration of the catalysts[13-17]. Besides the composition, the amount of active sites of the catalyst is another essential feature[18,19]. Typically, materials with 3-dimensional (3D) porous structure always possess a larger surface-area-to-volume ratio and more active sites than their lower-dimensional structures (i.e., 0D nanoparticles, 1D nanowires, and 2D nanosheets)[18,19], thus are expected to exhibit better catalytic performance. Due to the easy processability, wet-impregnation and precipitation methods by now have been the dominating

methods for synthesizing pre-catalysts[13,15-17]. In these methods, the catalyst precursors (e.g., nitrate salts) were mixed with large amounts of support materials in an organic solvent (e.g., ethanol), followed by drying and calcination at an elevated temperature[13,15-17]. A critical drawback of these methods is that the physical blending approach always limits the structural design of pre-catalysts, prohibiting the construction of active site-rich structures and leading to poor homogeneity of pre-catalysts. Besides, incorporating a significant fraction of support materials always leads to a poor surface-area-to-volume ratio due to the dense structure and formation of catalyst/support materials interfaces. Hence, a high catalyst-to-feedstock ratio had to be employed in the thermo-catalytic process (S. Table 1)[20], which seriously limited the industrial application. Moreover, the incorporation of large amounts of support materials also complicated the purification process of CNTs from the CNCs after the conversion. Therefore, to solve these bottlenecks there is a need for new composition-structure design paradigms if new catalysts possess not only a larger amount of active sites but also can be in situ formed with the proper supporting material.

Cobalt possesses excellent catalytic activity and has been widely used as a catalyst for the catalytic growth of CNTs[21-25]. MnO, as one of the most effective promoters, can significantly promote the catalytic dissociation efficiency of hydrocarbons (e.g., CH_4)[26,27]. Besides, MnO could not only increase the amount of active sites by weakening the catalyst/support material interface, but also stabilize the catalysts by inhibiting agglomeration and sintering[26,27], which avoid the incorporation of large amounts of inert support materials (e.g., γ/α-Al_2O_3, SiO_2, and zeolites). From these aspects, the Co/MnO materials are promising catalyst candidates by combining the advantages of the Co and MnO phases. However, the establishment of active-site rich structure and precise design of composition with excellent homogeneity of Co/MnO catalyst is challenging. The application of spinel phases with the general formula AB_2O_4, where *A* and *B* are metal ions (Fe, Co, Ni, Mn, etc.) [28,29], as a smart pre-catalyst which can self-convert into the targeted active-site-rich

catalysts will allow for such a combination of the required properties in just one material. The spinel structure can host cations with variable and various oxidation states and having design techniques in place to precisely control composition, morphology, and surface area[28-32], which enables the compositional design at the molecular level and establishment of active site-rich structure. For the recycling of waste plastic by pyrolysis-catalysis conversion, $Co_xMn_{3-x}O_4$ spinels are the ideal pre-catalysts, as they can not only meet the aforementioned requirements but also be facilely converted into the targeted Co/MnO catalyst[28,33].

In this work, multiscale designed 3D $Co_xMn_{3-x}O_4$ spinels possessing precisely adjusted composition and active site-rich structure that can self-convert into the targeted active site-rich Co/MnO catalysts were developed as smart pre-catalysts for the high-efficiency conversion of waste plastics. The microstructure design of catalysts was realized at the molecular level by hydrothermal synthesis of advanced $Co_xMn_{3-x}O_4$ spinels, while the active site-rich structure was simultaneously established by constructing a 3D rose-like structure. The catalytic performance of Co/MnO catalysts in relation to CNCs and H_2 production was investigated with respect to the composition, catalytic reaction temperature, as well as the pre-catalyst-to-plastic ratio. Density functional theory (DFT) calculations were conducted to simulate the interaction and dissociation of hydrocarbons on the surface of the Co/MnO catalyst. Moreover, as the purification of the obtained CNCs to CNTs is at least challenging (if not impossible), it was tested how the CNCs resulting from the catalytic conversion can be directly used. For this purpose, they were selectively tested as LIB anode material.

2. Experimental procedures

2.1 Chemicals

Cobalt (II) acetate tetrahydrate ($C_4H_6CoO_4 \cdot 4H_2O$), manganese (II) acetate tetrahydrate ($C_4H_6MnO_4 \cdot 4H_2O$), polyvinyl pyrrolidone (PVP, molecular weight 40000 $g \cdot mol^{-1}$) and ethylene glycol were supplied by Sigma-Aldrich Chemical Company (Germany). No further purification of the chemical agents was conducted before the experiment.

2.2 Synthesis of $Co_xMn_{3-x}O_4$ spinels

In this work, the 3D rose-like $Co_xMn_{3-x}O_4$ spinels were synthesized via a hydrothermal method. To start with, for $CoMn_2O_4$ 0.33 g $C_4H_6CoO_4 \cdot 4H_2O$, 0.66 g $C_4H_6MnO_4 \cdot 4H_2O$, and 0.3 g PVP were dissolved in 35 mL ethylene glycol under vigorous stirring for 45 min at room temperature. Then, the solution was transferred into a PTFE-lined autoclave tube (50 mL) and heated up to 200 ◦C in a hot air circulation oven. After 3 h, the autoclave was taken out from the oven and cooled down to room temperature in air. The precipitates from hydrothermal synthesis were washed with deionized (DI) water for 5 times and then collected with centrifugation before frozen drying. The freeze-dried powders were finally calcinated at 500 ^oC under ambient air atmosphere in a muffle furnace for 3 h. The obtained product was $CoMn_2O_4$ spinel. In this work, other batches of spinel-type oxides (i.e., $Co_{1.5}Mn_{1.5}O_4$, Co_2MnO_4, and $Co_{2.5}Mn_{0.5}O_4$) were also prepared. The $Co_{1.5}Mn_{1.5}O_4$, Co_2MnO_4, and $Co_{2.5}Mn_{0.5}O_4$ spinels were synthesized by varying the molar ratio of Co/Mn in ethylene glycol solvent under other identical experimental conditions. Based on the molar ratio of Co to Mn in spinels, the $CoMn_2O_4$, $Co_{1.5}Mn_{1.5}O_4$, Co_2MnO_4, and $Co_{2.5}Mn_{0.5}O_4$ spinels derived catalysts were named as Cat.-Co_1Mn_2, Cat.-$Co_{1.5}Mn_{1.5}$, Cat.-Co_2Mn_1, and Cat.-$Co_{2.5}Mn_{0.5}$, respectively.

2.3 Pyrolysis-catalysis conversion

In this work, model polyethylene was employed as the plastic feedstock. No further purification was conducted before the experiment. The elemental analysis result shows that the carbon,

hydrogen and nitrogen contents amount is 87.05 wt.%, 12.47 wt.% and 0.24 wt.%, respectively. The pyrolysis-catalysis recycling of waste plastics was conducted in a modified two-stage reactor[14-17, 34]. The experimental setup consists of two connected Al_2O_3 tube furnaces (one for pyrolysis and another for catalysis) and a gas supply system. In this part, pyrolysis-catalysis conversion reactions with varied parameters, including catalyst composition, the weight ratio of catalysts to waste plastics, and the catalytic reaction temperatures (e.g., 750 °C, 800 °C, and 850 °C) were performed, respectively. For the pyrolysis-catalysis reaction, the respective pre-catalyst will be spread on the Al_2O_3 bed reactor and placed in the center of the second-stage furnace for the catalytic reaction. An Al_2O_3 crucible with waste plastics (spent polypropylene) will be placed in the center of the pyrolysis furnace (first-stage). Before the plastic is heated, the catalysis furnace will be preheated to the set temperature (750 °C, 800 °C, or 850 °C). The plastics will be heated at a heating rate of 20 °C/min from 50 °C to 600 °C and held at 600 °C for 1 h in Ar atmosphere. During the catalytic transformation, the condensable large molecules from the decomposed plastics will be trapped in a condensing system cooled with an ice/water mixture, which can purify the hydrogen-rich gases and protect the equipment from contamination. The non-condensable gases will be collected with a Tedlar gas sample bag and analyzed with a gas chromatograph (GC). The GC is a dual channel system equipped with Channel A analyzing H_2, CO, and CH_4 using a molecular sieve 5A column with thermal conductivity detection (TCD) and channel B analyzing CO_2, C_2H_2, C_2H_4, and C_2H_6 with a polystyrene column and TCD[25]. The reproducibility of the experimental system is examined, and experiments are repeated to ensure reliability.

2.4 Materials characterization

Scanning electron microscopy (SEM) (S-4700, Hitachi, 15 kV) was used to study the morphology of the $Co_xMn_{3-x}O_4$ spinels and CNCs. The 3D structure of the $Co_xMn_{3-x}O_4$ spinels were observed

with transmission electron microscopy (TEM) (JEM2100F, JEOL). Lattice fingerprint of the $Co_xMn_{3-x}O_4$ spinels after H_2 reduction, and CNCs were characterized with transmission electron microscopy (F200X, FEI Tecnai, 200 kV). X-ray diffraction (XRD) (X'Pert Pro, Philips, Netherlands) of the $Co_xMn_{3-x}O_4$ spinels and CNCs was carried out with a STOE X-ray diffractometer in transmission geometry (Cu Kα1 radiation). The crystal structure of the $Co_{1.5}Mn_{1.5}O_4$ and $Co_{2.5}Mn_{0.5}O_4$ spinels after temperature programmed reduction at 550 °C was characterized by a STOE STADI MP (STOE GmbH & Cie, Darmstadt, Germany) X-ray diffractometer in a transmission geometry (Mo Kα1 radiation). Raman spectra were record from 500 cm^{-1} to 3000 cm^{-1} with a micro-Raman HR8000 spectrometer (Horiba JobinYvon, Bensheim, Germany) with a laser wavelength of 514.5 nm to characterize the graphitic degree of CNCs. Temperature programmed reduction (TPR) of the $Co_xMn_{3-x}O_4$ spinels were performed via a thermogravimetric analyzer (STA449F3, Netzsch Gerätebau GmbH, Selb, Germany) in a reductive atmosphere (5 vol.% H_2/95 vol.% Ar) with a heating rate of 10 $K \cdot min^{-1}$. The weight loss behavior of the CNCs as a function of temperature was characterized by temperature-programmed oxidation (TPO) by the thermal gravimetrical analysis and differential thermal analysis (TGA–DTA) using a high temperature simultaneous thermal analyzer (STA449F3, Netzsch Gerätebau GmbH, Selb, Germany). All measurements were corrected for buoyancy. The specific surface area was acquired according to the results of N_2 adsorption/desorption measurements at 77 K by an Autosorb-3B Analyzer (Quantachrome Instruments Corporation). Information on oxidations states, chemical boning environment, and composition of the $Co_xMn_{3-x}O_4$ samples before and after H_2 reduction were obtained with XPS. All experiments were performed within a vacuum-cluster tool (ULVAC-PHI *VersaProbe II) with* a pressure in the analysis chamber better than $5 \cdot 10^{-9}$ mbar. For excitation, monochromatic Al K_α radiation (1486.6 eV) was used. All detail spectra have been measured by applying a pass-energy of 23.5 eV. A step size of 0.1 eV/step was used. The backgrounds of the

acquired spectra were subtracted by using the Shirley method in CasaXPS [35], version 2.3.25. Samples were pressed into indium foil. Detailed spectra were normalized to maximum peak intensity and calibrated by setting C 1s to 284.5 eV for comparison.

2.5 Preparation of anode and electrochemical characterization

A mixture of the resulting CNCs, conductive carbon black (Timical Super C_{65}, Switzerland) and polyvinylidene fluoride (PVDF) (Arkema, France) were homogeneously mixed at a weight ratio of 8:1:1 in an agate mortar. *N*-methyl-2-pyrrolidinone (NMP; anhydrous, Sigma-Aldrich) was used as a solvent of the CNCs composite slurry. Prior to the preparation of the composite slurry, no further purification of the as-prepared CNCs was conducted. The slurry was cast onto a 100-µm-thick copper sheet and spread with a doctor blade coater. The electrode sheet was dried in a vacuum oven at 80 °C overnight to remove any solvent. The coin cells were assembled with CNCs anode and a lithium chip cathode using a Celgard 2325 separator, and were filled with 1 M $LiPF_6$ in EC/EMC (3:7 v/v) as the electrolyte. Electrochemical testing was carried out with a BCS-805 Biologic battery cycler (Biologic, France) at the charge/discharge current rate of 0.1 $A \cdot g^{-1}$ to measure the electrochemical capacity and life cycle. Cyclic voltammograms (CV) were performed on an electrochemical workstation (Interface 1000E, Gamry Instruments) at 0.1 $mV \cdot s^{-1}$ within the potential range of 0.01-3.0 V.

2.6 DFT calculations

The geometry optimizations and adsorption free energy calculations were performed by spin polarized DFT within the Hubbard U approach in the *Vienna* Ab initio simulation *package* (VASP) 5.4.4[36-38]. The projector augmented wave (PAW) potentials were employed and an energy cutoff of 500 eV was used[39]. The generalized gradient approximation (GGA) with the Perdew-Burke-

Ernzerhof (PBE) function was adopted for the exchange-correlation potentials, and value of U was set as 2.0 eV and 5.0 eV for Co 3*d* and Mn 4*f*, respectively. The Brillouin zone was sampled on a Monkhorst-Pack *k*-point mesh of 2 × 2 × 1. The energy and force convergence criterion were set as 10^{-4} eV and 0.03 eV·$Å^{-1}$.

3. Results and discussion

3.1 Characterization of the spinel pre-catalysts

Fig. 1a schematically shows the upcycling procedure of waste plastic via the pyrolysis-catalysis method. (Co,Mn)-based spinels with 3D rose-like morphology were prepared via a hydrothermal method. The 3D structure enables the construction of active site-rich structures. This provides more accessible surface area for the hydrocarbons (e.g., CH_4, C_2H_4, and C_2H_6) from the decomposition of plastic wastes, which will lead to a strong capturing capability of the hydrocarbons. Through reaction on the catalyst surface, the hydrocarbons were converted into H_2 and CNTs. No further purification was applied and the resulting CNCs were directly tested as lithium battery anode material. Fig. 1b-1h present the typical SEM and TEM images and XRD patterns of as-prepared spinels after annealing at 500 $^{\circ}$C for 3 h. In the low magnification SEM image, $CoMn_2O_4$ particles with a size of 3 μm were individually dispersed. In the high magnification SEM image (Fig. 1c), $CoMn_2O_4$ spinel with a 3D rose-like porous structure was observed. As we can see, 2D $CoMn_2O_4$ spinel nanosheets with a thickness of about 60 nm were self-assembled into a 3D structure. This structure significantly benefits the material as pre-catalyst by exposing more active sites and accessible surface area to the hydrocarbon gases released by the decomposed plastics. In the references [16,17], the authors report on the development of a highly porous structure to obtain large specific surface areas of the catalyst systems. For example, highly porous zeolites with a large specific surface area (≥200 m^2/g) was employed as the carrier of the catalyst[16]. However, some nano/submicro scaled pores are not accessible for the large hydrocarbon molecules or are easily blocked by the precipitated carbon, leading to the deactivation of the catalyst. In this circumstance, a large plastic-to-catalyst weight ratio (2:1) has to be employed. For pyrolysis-catalytic recycling,

the active sites and accessible surface area are necessary factors for a highly efficient conversion. In this work, 3D flower-like materials composed of 2D nanosheets were developed as pre-catalyst. This network structure will significantly enhance the active sites and accessible surface area for the hydrocarbon gases from the decomposed plastics. Instead of growing in the pores with limited space, the carbon nanotubes can directly grow on the surface of the 2D flat nanosheets to the free space (Fig. 1a).

In this work, the polyvinylpyrrolidone (PVP), as a surfactant and complexing agent is critically important for the establishment of the 3D porous structure. As a complexing agent, the Co and Mn ions were absorbed onto the hydrophilic carbonyl groups of PVP during the complexing process. The hydrophobic vinyl and hydrophilic carbonyl groups on the PVP could lead to polarized micelles, which as a result would lead to the shape-inducing effect[40,41]. As a surfactant, the PVP can agglomerate the primary particles composed of the metal complex on the surface of polarized micelles. Due to the shape-inducing effects, these particles were shaped into flat 2D nanosheets, and gradually packed into the observed 3D structure. After calcination in air, the PVP was removed, while the pristine 3D porous structure was retained owing to the spherical blocking effect[40,41]. Interestingly, regardless of the Co/Mn molar ratio in the resulting $Co_xMn_{3-x}O_4$ spinels, the materials always exhibit a 3D rose-like structure (S1), which can be attributed to the facile tunability of Mn and/or Co ions in the $Co_xMn_{3-x}O_4$ spinel due to the variable valence of both Co (+2/+3) and Mn (+2/+3) ions. In the XRD patterns of $CoMn_2O_4$, $Co_{1.5}Mn_{1.5}O_4$, Co_2MnO_4, and $Co_{2.5}Mn_{0.5}O_4$ spinels, the characteristic diffraction peaks corresponding to lattice planes (101), (112), (200), (103), (211), (220), (321), (224), and (400) were detected, confirming the formation of $Co_xMn_{3-x}O_4$ spinels[42-44]. Moreover, with the increase of the Co/Mn molar ratio in the spinels, the characteristic (211) diffraction peak was found to shift to a larger angle due to smaller ionic radios of Co compared to Mn assuming the same oxidation state[45]. In the low-resolution TEM image, a porous Co_2MnO_4

particle with a bottom-up status was observed, in which the petals of the spinel follower were found to be vertical and parallel to the TEM sample grid. Moreover, some pores with nanoscale level were also observed in the petal in Fig. 1f and the thickness of vertical follower petals varied between 40-60 nm. In the high-resolution TEM image (Fig. 1g), the lattice space was measured to be 0.294 nm, matching the (220) plane of Co_2MnO_4 spinel[46], which also agrees well with the lattice spacing from XRD. In the EDX mappings (Fig. $1h_2$-$1h_3$), strong signals from Mn, Co, and O elements were detected in the overlapping area of the STEM image in Fig. $1h_1$, confirming the existence of the Mn and Co elements. As expected, the Mn and Co mapping area overlapped well with each other in the detected area, which further confirms the formation of the Co_2MnO_4 spinel. Due to the high Co content in Co_2MnO_4, the signal of Co is obviously stronger than that of Mn in the EDX mapping, which is different from the EDX mapping of $CoMn_2O_4$ in S.2.

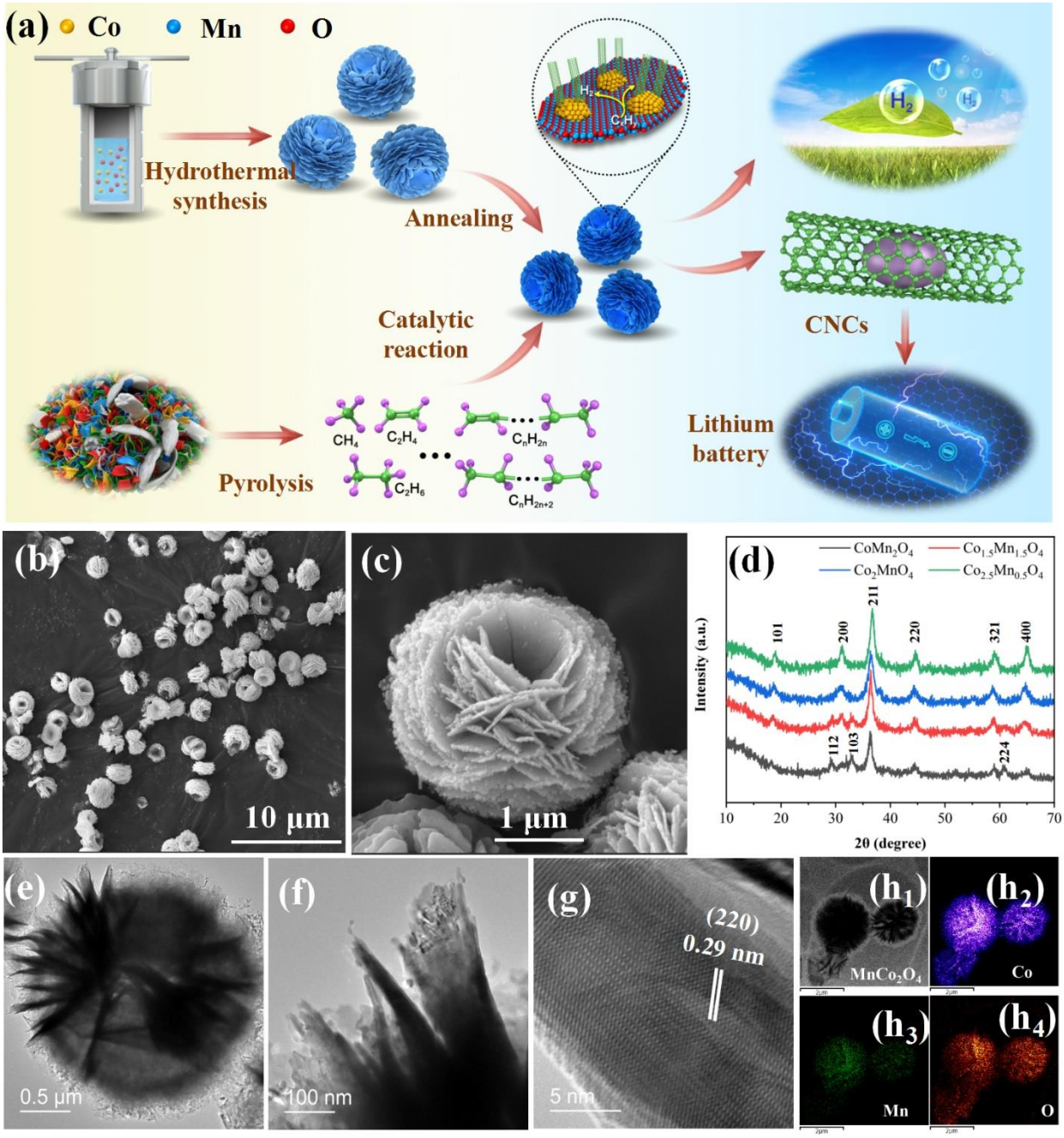

Fig. 1 (a) Schematic illustration of upcycling procedure of waste plastic with the rose-like catalysts, (b) and (c) low and high magnification SEM images of $CoMn_2O_4$, (d) XRD patterns of $CoMn_2O_4$, $Co_{1.5}Mn_{1.5}O_4$, Co_2MnO_4, and $Co_{2.5}Mn_{0.5}O_4$, (e) low, (f) and (g) high resolution TEM images of Co_2MnO_4, (h_1) STEM image of Co_2MnO_4, (h_2), (h_3) and (h_4) EDX mapping of Co, Mn, and O.

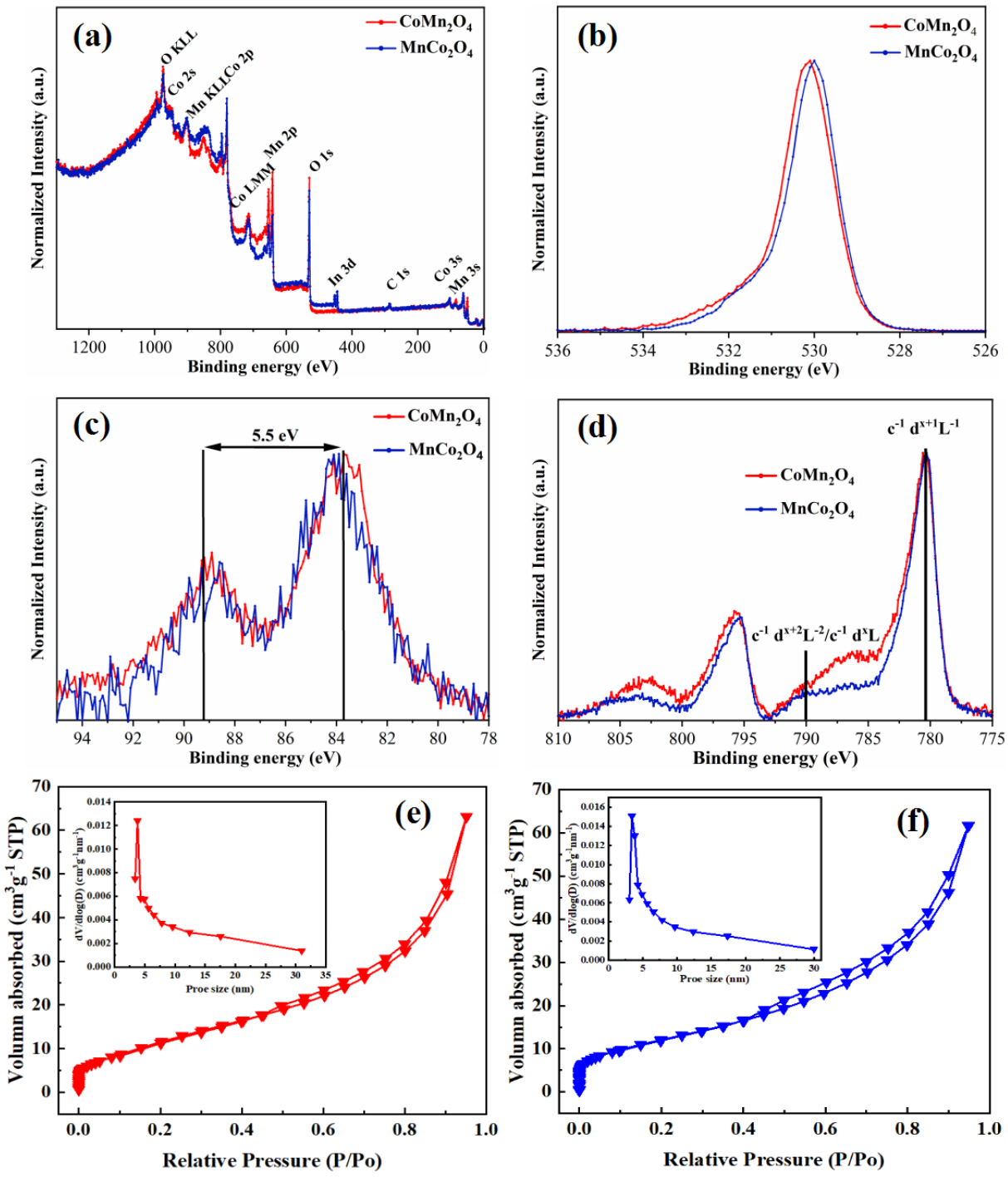

Fig. 2 (a) XPS survey spectra of $CoMn_2O_4$ and $MnCo_2O_4$, (b) O 1s spectra of $CoMn_2O_4$ and $MnCo_2O_4$, (c) Mn 3s spectra of $CoMn_2O_4$ and $MnCo_2O_4$, and (d) Co 2p spectra of $CoMn_2O_4$ and $MnCo_2O_4$, N_2 adsorption/desorption isotherms of spinels of (e) $CoMn_2O_4$ and (f) Co_2MnO_4, inserts show the distributions of the pore size in corresponding spinels.

Further information with respect to chemical environment, oxidation state, and composition of the spinels before and after H_2 reduction was obtained by X-ray photoelectron spectroscopy (XPS), Brunner−Emmet−Teller (BET) method, thermal gravimetrical analysis and differential thermal analysis (TGA–DTA) (Fig. 2 and Fig. 3). In the survey XPS spectra of $CoMn_2O_4$ and Co_2MnO_4 (Fig. 2a), all expected elements were detected, which agrees well with the TEM EDX mapping results. The O 1s spectra show the same shape for both materials with the position at 530 eV which is typical for metal oxides. In the Mn 3s spectra of $CoMn_2O_4$ and $MnCo_2O_4$ (Fig. 2c), the main peak of Mn was detected at 83.9 eV and the splitting for both samples was found to be 5.5 eV. The two final states occur due to the coupling of the remaining 3s electrons to the 3d electrons upon ejection of the 3s electrons[47,48]. Based on the splitting, the Mn is indicated to be in a 3+ state in both samples.

The Co 2p spectra can be understood in terms of charge transfer effects[49]. Next to the spin-orbit splitting of the peaks (Fig. 2d), satellites occur next to the main peaks. The main peak at BE (Co $2p_{3/2}$) = 780 eV can be characterized by the $c^{-1}d^{x+1}L^{-1}$ configuration. Where c denotes the core hole and $d^{x+1}L^{-1}$ the charge transfer from the ligand to the d-orbital. The satellite peak at 790 eV corresponds to the $c^{-1}d^{x}L$ configuration where the 2p core electron is ejected and the ligand stays intact (Fig. 2d). It is assumed that at this energy also a $c^{-1}d^{x+1}L^{-2}$ process occurs in which the ligand loses two electrons[50,51]. Additionally, another satellite occurs at ca. 786 eV. No direct charge transfer process is defined for this satellite. However, this satellite is mainly seen in CoO and thus the satellite can be associated with Co^{2+}[52]. In $CoMn_2O_4$, the intensity of this satellite is high, which indicates cobalt is in a +2 state, while in $MnCo_2O_4$ cobalt is in a mixed +2/+3 (average +2.5) state. This finding is in good agreement with the expected oxidation state and also the 3+ state of Mn in both samples, which means that the distribution of Co and Mn between A- and B- site might change as well.

N_2 adsorption/desorption isotherms of $CoMn_2O_4$ and $MnCo_2O_4$, as representative samples were presented to analyze the porosity of the prepared spinel pre-catalysts (Fig. 2e and 2f). As shown, the isotherms of $CoMn_2O_4$ and $MnCo_2O_4$ obey the Type IV characteristic feature and therefore, indicate the formation of mesopores in the petals of spinels, agreeing well with the observation in the TEM images (Fig. 1f and S. 2a). From the inserting images we can see that the pore size in the petals of $CoMn_2O_4$ and $MnCo_2O_4$ locates mainly at ~3.8 nm, the typical range of mesopores. Regardess of the Co,Mn ratio in the spinels, always similar specific surface area value (~50 m^2/g) were exhibited, this can be attributed to the same morphology and particle size of prepared spinels (Fig. 1 and S.1).

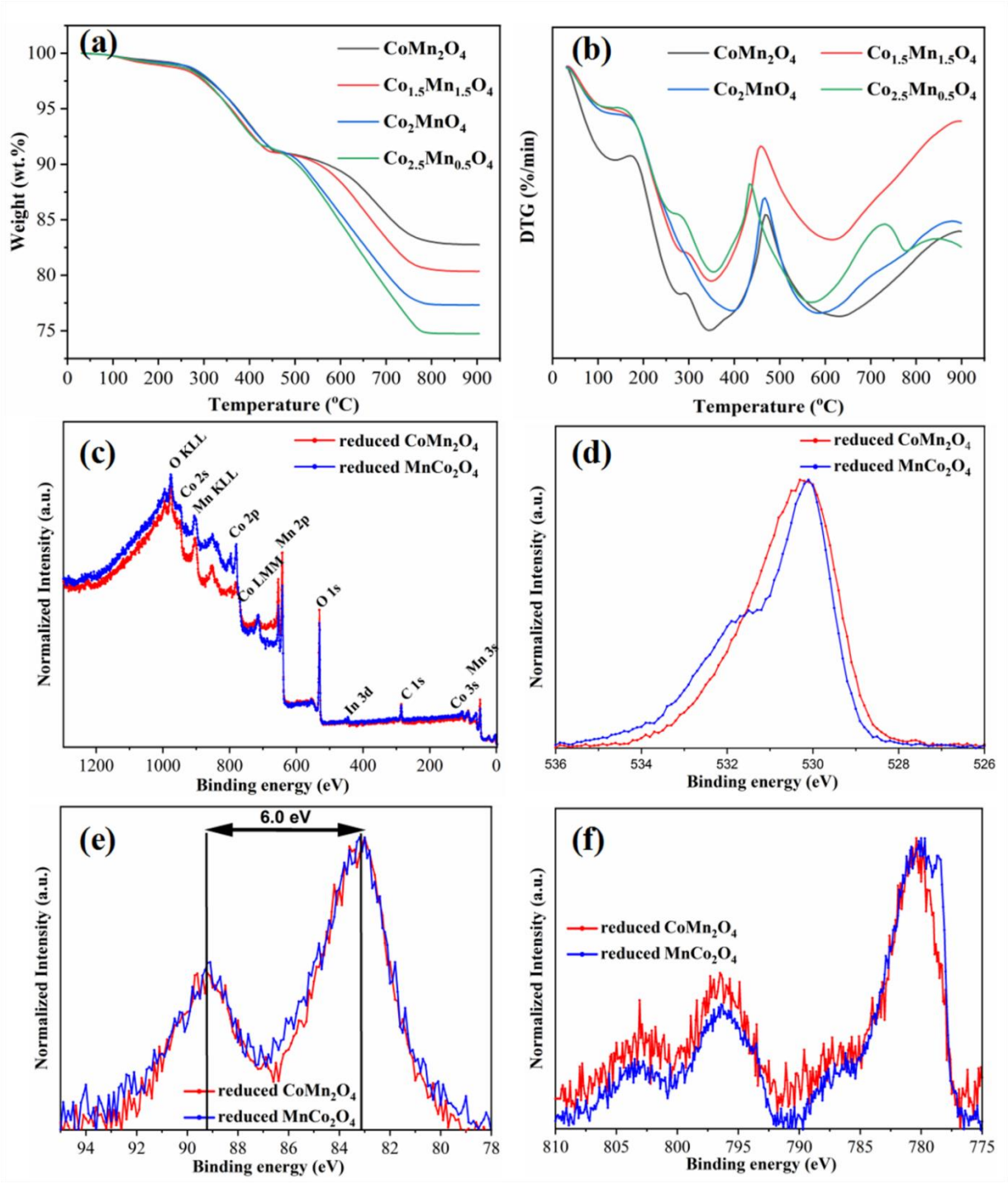

Fig. 3 (a) Temperature programmed reduction and (b) derivative plots of pre-catalysts at a heating rate of 10 $^{\circ}C \cdot min^{-1}$ in 5 vol.% H_2 in Ar of all batches of spinels (c) XPS survey spectra of reduced $CoMn_2O_4$ and $MnCo_2O_4$, (d) O 1s spectra of reduced $CoMn_2O_4$ and $MnCo_2O_4$, (e) Mn 3s spectra of reduced $CoMn_2O_4$ and $MnCo_2O_4$, (f) Co 2p spectra of reduced $CoMn_2O_4$ and $MnCo_2O_4$.

Fig. 3a and 3b are the thermogravimetric (TG) and differential thermogravimetric (DTG) curves of the spinel pre-catalysts as a function of reduction temperature. As shown in Fig. 3a, the spinels exhibited increased weight loss with the increase of Co/Mn ratio in the spinels and reduction temperature. Based on the TG and DTG curves, the weight loss behavior of spinels can be divided into three stages. The first stage happened at the temperature range of lower than 200 °C, which is resulted from the evaporation of absorbed water molecular in the spinels. At the first stage, a weight loss of ~1.5 wt.% occurred. The second stage occured between 300-400 °C. Interestingly, regardless of the Co/Mn ratio in spinels, the weight loss at this stage is almost the same. We suggest this phenomenon can be attributed to the reduction of Co^{2+} at the A-site of spinels into metallic Co (S. 3). At the second stage, the weight loss is 7.5-8.0 wt.%, which agrees well with the theoretical oxygen content change induced by A-site cation reduction. The third stage mainly happened between 500-750 °C, which is resulted from the reduction of transition metal ions at the B-site. Based on the calculation, the overall weight loss after reduction is always lower than the theoretical oxygen content in spinels. For example, the theoretical oxygen content in $CoMn_2O_4$ is 27.5 wt.%. However, after reduction in 5 vol.% H_2 a weight loss of ~15.0 wt.% was obtained. During the reduction, the Co^{2+} ions in the spinels were reduced into metallic Co, while the Mn ions were reduced from +3 state to +2 state, pointing to a formation of MnO.

Fig. 3c-3f present the XPS spectra of the $CoMn_2O_4$ and Co_2MnO_4 after reductive thermal treatment. As expected, Mn, Co, and O elements were detected in the survey XPS spectra of the reduced $CoMn_2O_4$ and Co_2MnO_4 (Fig. 3c). The O 1s spectra show the same shape for both materials with the position at 530 eV which is typical for metal oxides like pristine materials. Additionally, the peaks are broadened and in $CoMn_2O_4$ a clear shoulder is visible, indicating the formation of metal carbonates or organic C-O bonds (Fig. 3d). After reduction with H_2, the Mn 3s spectra showed the main peak at 83.2 eV and splitting of ca. 6.0 eV for both samples (Fig. 3e). This

indicated that Mn changed from a +3 to +2 state, which agrees well with the TG results. In Fig. 3f, a strong broadening of the Co $2p_{3/2}$ main peak can be seen. One explanation could be the contribution of metallic cobalt with lower binding energies of 778.2 eV, which would overlap with the main peaks of the oxides. In contrast to the oxides, metallic cobalt has no satellite features, indicating that the majority of cobalt is still mainly in a 2+ or higher oxidation state. This can be explained by the partial oxidation of metallic Co on the surface of the Co/MnO catalyst and the low detection depth of XPS in the measured sample. In the high-resolution TEM image of H_2 reduced $MnCo_2O_4$, metallic Co particles with a size of 5-10 nm were found to be dispersed in the MnO matrix (S. 2e). Moreover, the lattice space of the exposed phase was measured to be 0.22 nm, matching well with the (200) crystal plane of MnO. In the EDX mapping, strong signals from Mn, Co, and O elements can still be found. However, different from the EDX mapping of the Co_2MnO_4 spinel, the homogeneity of the Co element was found to reduce. In S. 2f, the Co element was found to agglomerate after reduction. Moreover, by comparison, we can observe that in the overlapping areas where there is strong Co agglomeration the signal from the O element was weakened. This is resulted from the reduction of cobalt oxide and the formation of metallic Co particles, which can also be confirmed by the temperature-programed reduction plots of the $Co_xMn_{3-x}O_4$ spinels (Fig. 3a and 3b).

3.2 Products analysis

By now, carbon and H_2 yield (CY and HY) are commonly employed as the criterion for the evaluation of the conversion efficiency of waste plastics[16-17, 53-57]. High CY and HY always represent high conversion efficiency of plastics. The CY and HY can be determined by the following equations:

$$\mathrm{CY} = \frac{W_{car}}{W_{pla}} \quad (1)$$

$$\mathrm{HY} = \frac{n_{H2}}{W_{pla}} \quad (2)$$

where W_{car} represents the weight of deposited carbon on the catalysts, W_{pla} represents the weight of plastics, and n_{H2} represents the molar quantity of H_2. The W_{car} is determined by the weight difference between the fresh pre-catalyst and CNCs.

Fig. 4a-4c present the H_2 and carbon yield of plastics with respect to catalyst compositions, catalytic reaction temperature, and the weight ratio of catalyst to plastic. Fig. 4a shows the H_2 and carbon yield of plastics catalyzed by Cat.-Co_1Mn_2, Cat.-$Co_{1.5}Mn_{1.5}$, Cat.-Co_2Mn_1, and Cat.-$Co_{2.5}Mn_{0.5}$ at a temperature of 800 ˚C and with a pre-catalyst to plastic weight ratio of 1:20. As shown in Fig. 4a, the carbon and H_2 yield increased with the increase of the Co/Mn molar ratio in the catalyst up to 2:1. For Cat.-Co_1Mn_2 catalyst, when the weight ratio of catalyst to plastic is 1:20, the carbon and H_2 yield can reach as high as 35.6 wt.% and 22 mmol·$g_{pla.}^{-1}$, respectively. With the further increase of the Co/Mn molar ratio to 2:1, the catalyst exhibited its best catalytic performance in relation to carbon and H_2 yield (Fig. 3a and S. 4), which is 37.4 wt.% and 32 mmol·g_{pla}^{-1}. However, when the Co/Mn molar ratio increased to 2.5:0.5, the carbon and H_2 yield decreased significantly to 14.4 wt.% and 16 mmol·$g_{pla.}^{-1}$, which can also be confirmed by the temperature-programmed oxidation plots of CNCs (S. 4). This phenomenon can be explained by the agglomeration of Co catalyst at too low MnO content (S. 5k and 5l). In this work, the reduced Co nanoparticles, as an active material, catalyzed the conversion of the hydrocarbons into H_2 and carbon nanotubes. With the increase of Co/Mn molar ratio in the catalyst from 1:2 to 2:1, the amount of Co catalyst increased accordingly, which could lead to more hydrocarbons being captured and increasing the amount of CNTs and H_2. During the catalytic reaction, the

simultaneously formed MnO acted as a carrier to immobilize the Co catalyst and prevent it from deactivation. When the Co/Mn molar ratio is higher than a certain ratio (2.5:1 in this work), agglomeration of the catalyst occurs, which leads to the decrease of catalytic activity and production yield of CNTs and H_2, respectively. When the content of MnO in the catalyst is lower than a certain threshold value, agglomeration of the Co catalyst occurres, which leads to the decrease of accessible surface area for the hydrocarbons and prohibits the growth of CNTs (S. 5l). Meanwhile, from the SEM images, we can see that the diameter of the CNTs exhibited an increasing tendency with the increase of the Co/Mn molar ratio (S. 5), which we suggest is resulted from the increased particle size of the Co catalyst. Moreover, due to the agglomeration of Co element in the Cat.-$Co_{2.5}Mn_{0.5}$ catalyst, the CNTs in S. 5l exhibited a decreased length compared to the CNTs prepared by other catalysts. Besides the catalyst composition, the reaction temperature is another important factor that influences the catalytic performance of the catalyst. In this work, the catalytic performance of the Cat.-Co_2Mn_1 catalyst was investigated with respect to the variation of temperature (750 $^{\circ}$C-850 $^{\circ}$C) (Fig. 4b). With the increase of reaction temperature from 750 $^{\circ}$C-850 $^{\circ}$C, the variation of carbon and H_2 yield of Cat.-Co_2Mn_1 exhibited a parabolic tendency. At the temperature of 750 $^{\circ}$C, the carbon and H_2 yield can reach 35.0 wt.% and 26.5 mmol·g_{pla}^{-1}, which is lower than that of the Cat.-Co_2Mn_1 catalyst exhibited at 800 $^{\circ}$C. However, when the temperature increased to 850 $^{\circ}$C, the carbon and H_2 yield decreased to 33 wt.% and 28.3 mmol·g_{pla}^{-1}. This phenomenon can be explained by the decreased catalytic activity resulting from the agglomeration or sintering of the catalyst at a high temperature (see the big particles in S. 6g). By comparing the carbon and H_2 yield (Fig. 4b and S. 7), the Cat.-Co_2Mn_1 exhibited the best catalytic performance at the temperature of 800 $^{\circ}$C. To maximize the upcycling efficiency, the carbon and H_2 yield of plastic as a function of Cat.-Co_2Mn_1 catalyst to plastic weight ratio was also investigated. Fig. 4c presents the carbon and H_2 yield of Cat.-Co_2Mn_1 as a function of catalyst to plastic ratio

weight ratio when catalyzing at 800 °C. As expected, the carbon and H_2 yield increased with the increase of catalyst/plastic weight ratio (Fig. 4c and S.9). As shown in Fig. 4c, even at an extremely low weight ratio of catalyst to plastic ratio of 1:40, the carbon and H_2 yield of Cat.-Co_2Mn_1 can still reach as high as 23 wt.% and 22.3 mmol·g_{pla}^{-1}, which proved the excellent catalytic performance of our catalyst. When the catalyst to plastic weight ratio increased to 1:14, the carbon and H_2 yield reached 41 wt.% and 36 mmol·$g_{pla.}^{-1}$, which is even comparable to the carbon and H_2 yield of reported work with ultrahigh catalyst/plastic weight ratio (1:2) (S. Table 1)[17,53].

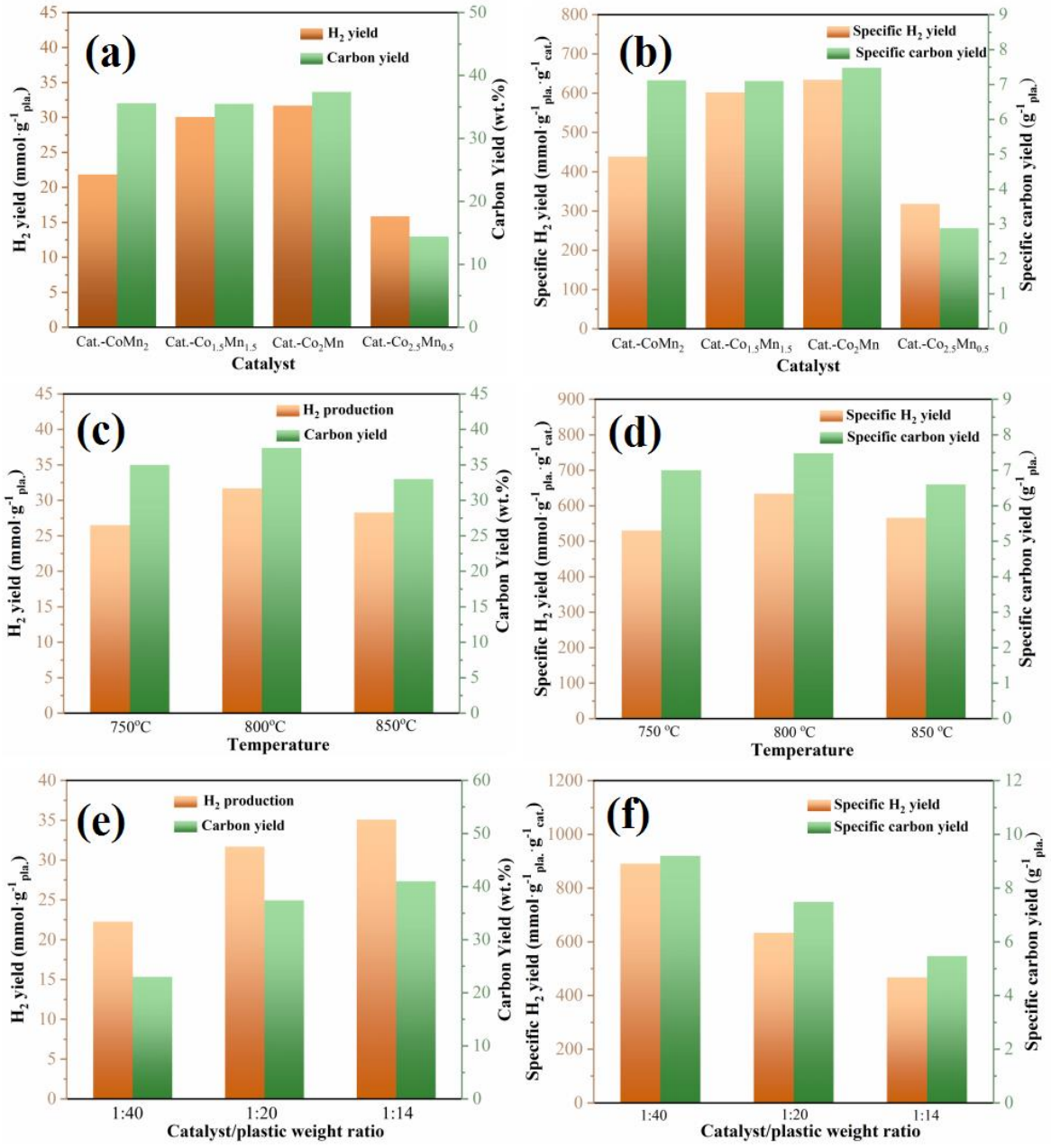

Fig. 4 H_2 and carbon yield derived from: (a) Cat.-Co_1Mn_2, Cat.-$Co_{1.5}Mn_{1.5}$, Cat.-Co_2Mn_1, and Cat.-$Co_{2.5}Mn_{0.5}$ at a temperature of 800 ˚C, (b) Cat.-Co_2Mn_1 at different temperatures from 750 ˚C to 850 ˚C, (c) Cat.-Co_2Mn_1 with different weight ratios of catalyst to plastic; and specific carbon and hydrogen yield of (d) Cat.-Co_1Mn_2, Cat.-$Co_{1.5}Mn_{1.5}$, Cat.-Co_2Mn_1, and Cat.-$Co_{2.5}Mn_{0.5}$ at a temperature of 800 ˚C, (e) Cat.-Co_2Mn_1 at the temperature range of 750 ˚C -850 ˚C, and (f) Cat.-Co_2Mn_1 with the catalyst weight ratio of 1:40, 1:20, and 1:14 when catalyzing at 800 ˚C.

Besides high CY and HY, the amount of catalysts employed in the upcycling process should also be considered in industrial applications in particle since the catalyst can get disseminated to CNCs. In this circumstance, CY and HY alone will not be sufficient for the comprehensive evaluation of the overall conversion performance, since higher CY and HY can be easily achieved by employing a larger amount of catalysts, which directly increases the upcycling costs and challenges of the purification of the CNTs. A more reasonable way is to use more reliable parameters, namely specific carbon and H_2 yield (SCY and SHY), that are the CY and HY divided by the weight of the pre-catalyst. Such parameters are highly valuable for determining the overall conversion efficiency by incorporating three important factors: the carbon and H_2 yield as well as the weight of the pre-catalyst, which will be obtained from the following equations:

$$\mathrm{SCY} = \frac{\mathrm{CY}}{W_{\mathrm{cat}}} \tag{3}$$

$$\mathrm{SHY} = \frac{\mathrm{HY}}{W_{\mathrm{cat}}} \tag{4}$$

Fig. 4d shows the SCY and SHY of Cat.-Co_1Mn_2, Cat.-$Co_{1.5}Mn_{1.5}$, Cat.-Co_2Mn_1, and Cat.-$Co_{2.5}Mn_{0.5}$ at a reaction temperature of 800 ˚C with a catalyst/plastic ratio of 1:20. Due to the excellent catalytic performance of the catalysts, outstanding SCY and SHY values were obtained from the resultant catalyst materials. As shown in Fig. 4d, the SCY and SHY of Cat.-Co_1Mn_2 can reach as high as 7.12 $g_{cat.}^{-1}$ and 438 $mmol \cdot g_{pla.}^{-1} \cdot g_{cat.}^{-1}$, respectively, which is about one order of magnitude higher than the reported values (S. Table 1)[15,53]. With the increase of Co/Mn molar ratio, the SCY and SHY of the CoMn-based catalysts exhibited the same varying tendency than for CY and HY. Among all batches of catalysts, the Cat.-Co_2Mn_1 exhibited the highest SCY and SHY values of 7.48 $g_{cat.}^{-1}$ and 634 $mmol \cdot g_{pla.}^{-1} \cdot g_{cat.}^{-1}$. This outstanding performance can be attributed to the excellent catalytic activity and active site-rich structure of as-prepared smart 3D (Co,Mn)-based

spinel pre-catalyst. Moreover, the SCY and SHY values as a function of reaction temperature and catalyst amounts were also investigated. With the increase of catalyst weight, the carbon and H_2 yield increased while the SCY and SHY decreased. When the weight ratio of catalyst to plastic is 1:40, the SCY and SHY reached 9.2 $g_{cat.}^{-1}$ and 891 $mmol \cdot g_{pla.}^{-1} \cdot g_{cat.}^{-1}$. However, the morphology of CNTs did not exhibit obvious change with the variation of catalyst to plastic ratio (S. 8).

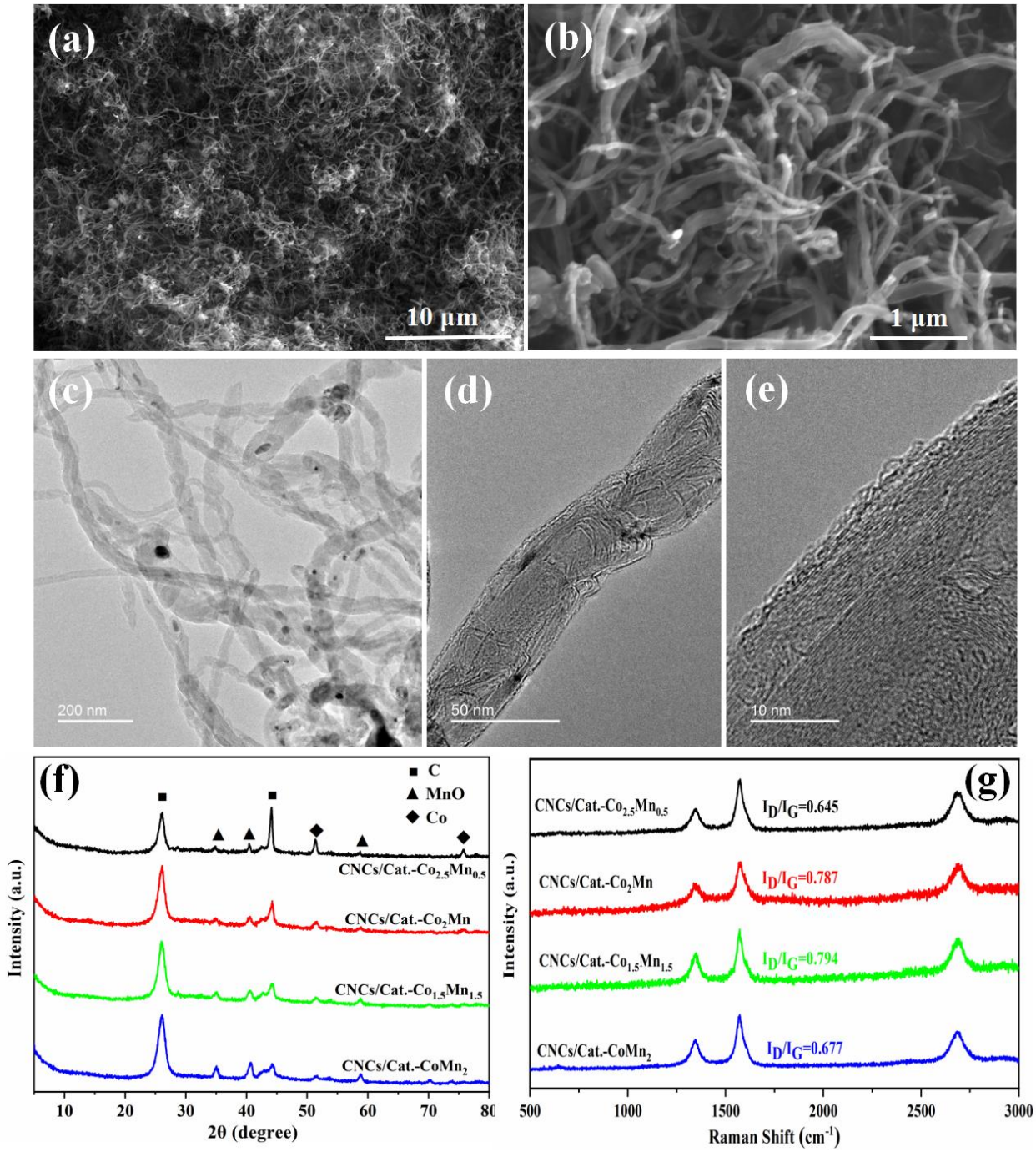

Fig. 5 (a) and (b) low and high magnification SEM images of CNCs catalyzed by Cat.-Co_1Mn_2 at a temperature of 800 ˚C, (c) low resolution TEM image of the aforementioned CNCs, (d) and (e) high-resolution TEM images of CNCs, (f) XRD patterns and (g) Raman spectra of the CNCs catalyzed by Cat.-Co_1Mn_2, Cat.-$Co_{1.5}Mn_{1.5}$, Cat.-Co_2Mn_1, and Cat.-$Co_{2.5}Mn_{0.5}$ at 800 ˚C.

Fig. 5a-5e show the representative SEM and TEM images of the deposited carbon. As shown in Fig. 5a, filamentous carbon materials with a length of more than 10 μm were observed. In the high magnification SEM image, we can see that the diameter of these materials is lower than 100 nm. The TEM images (Fig. 5c-5e) confirm the hollow tube structure of the filamentous carbon materials, which are known as CNTs. In the low-resolution TEM image (Fig. 5c), we can see that the hollow multi-walled CNTs possessed diameters of 30 to 70 nm. Different from the CNTs reported in literature possessing smooth outer surface, the CNTs obtained in this work exhibited a bamboo-like structure. In the high-resolution TEM images (Fig. 5d and 5e), the "joint" of the multi-walled CNTs is clearly observed. Moreover, in each "bamboo joint", catalyst particles with diameters of ~5 nm were found to insert in the multi walls of the CNTs. This phenomenon can be explained by the "particle-wire-tube" growth mechanism of CNTs [58,59].

The "particle-wire-tube" growth process can be divided into three stages, which are (a) precipitation of solid carbon by capturing gaseous carbon and aggregation into carbon nanoparticles, (b) growth of carbon nanowires by merging of the nanoparticles, (c) formation of the graphene-like carbon layers from the poorly graphitic carbon and formation of a hollow structure. By now, the most widely accepted growth mechanisms of CNTs are "top growth" and "bottom growth" mechanisms, where the gaseous carbon is captured by the catalyst particles, followed by the precipitation of solid carbon, and the growth of hollow tube on the bottom or top of the catalyst particles[13]. Typically, "top growth" or "bottom growth" mechanisms apply to these catalysts possessing relatively large particle sizes, which can provide a large enough growth driving force for the direct formation of the hollow tube structure[13, 58,59]. In this work, due to the molecular-level design method of the pre-catalyst, the reduced Co nano-particles were homogeneously dispersed in the MnO phase, which inhibited the growth of Co particle size. When the particle size of the catalyst is not large enough, the direct formation of a hollow tube resulting

from “top growth” and “bottom growth” mechanisms will be challenging and "particle-wire-tube" will be a dominant growth mechanism. Corresponding revisions were also made in the manuscript.

In the XRD patterns of CNCs (Fig. 5f and S.10), characteristic diffraction peaks of graphitic carbon, metallic Co, and MnO were detected. From the Raman spectroscopy (Fig. 5g and S. 11), we can find that the CNCs possess an excellent graphitic degree. Moreover, with the increase of catalytic reaction temperature, the graphitic degree of resulting CNCs increased (S. 11).

3.3 DFT calculations

DFT calculations are employed to understand the catalytic mechanism of the Co/MnOcatalyst. Before we carry out the DFT calculations, the characterization results of H_2 reduced catalysts (XPS in Fig. 3 and TEM in S. 2) and the final state of catalysts after pyrolysis-catalysis reaction (XRD in S. 10 and TEM in S.12 and S.13) were employed to support the construction of DFT calculation models. XPS and XRD results confirmed the presence of metallic Co and MnO in the catalysts. Moreover, based on the HRTEM images of the H_2 reduced Co_2MnO_4 (S.2e) and CNCs after catalytic reaction (S. 13 and S.13), the crystal plane (200) of MnO is the preferentially exposed surface of MnO phase. Meanwhile metallic Co particles with nanoscaled size were observed to disperse on the MnO phase. Different from single atom catalytic model[60-62], a Co cluster composed of 4 Co atoms (Co_4) was employed to simulate the Co particles in the Co/MnO catalyst. Thus, the Co/MnO catalyst model for the DFT calculations was established by supporting Co_4 on a MnO (200) surface (Fig. 6a). Methane (CH_4), ethane (C_2H_6), and ethylene (C_2H_4) were chosen as representative hydrocarbons from the depolymerization of plastic wastes. Different potential anchoring sites for Co nanoparticles on MnO were examined (Fig. 6 and S. 14). The most stable anchoring sites are shown in Fig. 6(a).

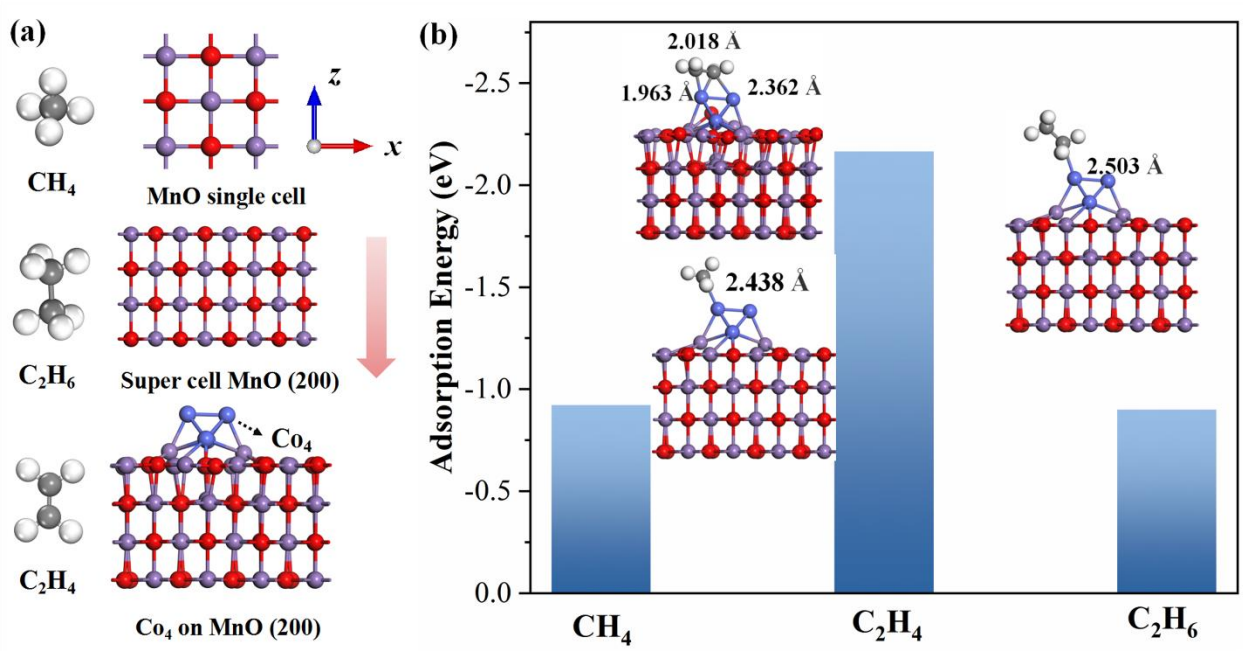

Fig. 6 (a) The surface structure model of Co/MnO catalyst and ball-and-stick models of CH_4, C_2H_4, and C_2H_6, (b) adsorption energy of CH_4, C_2H_4, and C_2H_6 on Co/MnO catalyst.

In the catalytic conversion, adsorption of hydrocarbons on the surface of the catalyst took place prior to the catalytic reaction. The corresponding adsorption energy of representative hydrocarbons (CH_4, C_2H_6, and C_2H_4) were calculated. As shown in Fig. 6b, based on the DFT calculations, the adsorption energy of hydrocarbons is ranked as: $C_2H_4 < CH_4 < C_2H_6$. Among these three hydrocarbons, C_2H_4 exhibited the lowest adsorption energy on the surface of the Co/MnO catalyst, which is as low as -2.2 eV. The low adsorption energy indicates that C_2H_4 is more strongly attracted compared to CH_4 and C_2H_6 on the Co/MnO catalyst[63]. Meanwhile, C_2H_6 and CH_4 almost exhibit the same level of adsorption energy. This phenomenon can be explained by a) the shortest length of C-Co bond of C_2H_4 among all these three hydrocarbons and similar length of the C-Co bond of CH_4 and C_2H_6 [63]; b) the C=C double bond in C_2H_4 while C-C bonds in C_2H_6 and CH_4; c) end-on adsorption of C_2H_6 and CH_4 in contrast to the side-on adsorption of C_2H_4.

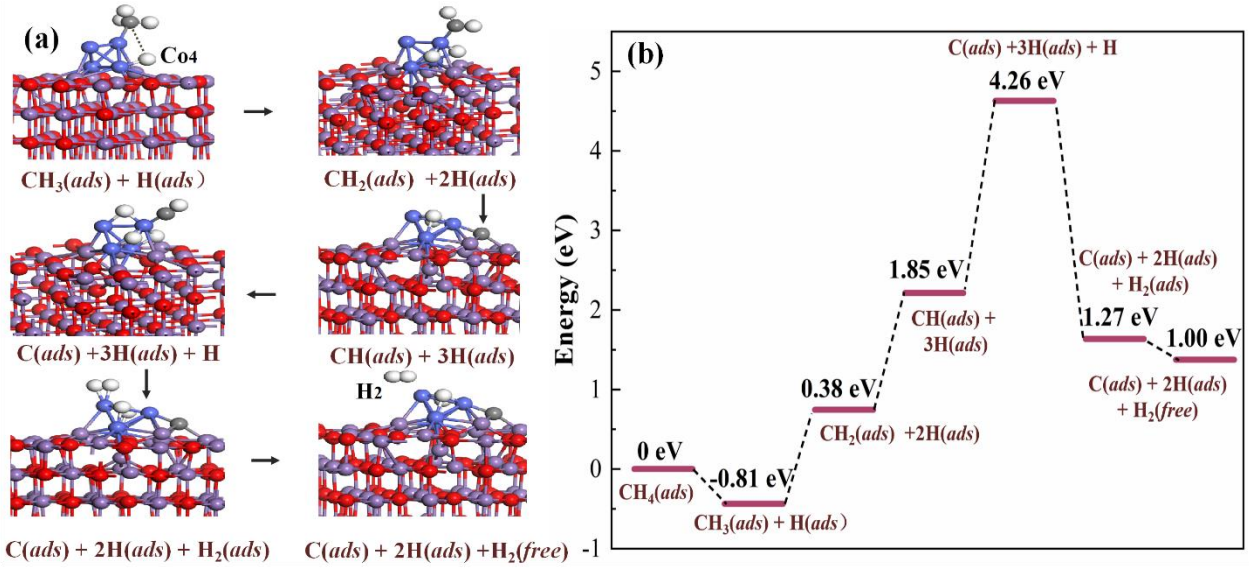

Fig. 7 (a) Transition state geometries of CH_4 dissociation on Co/MnO catalyst, (b) Gibbs free energy diagram from DFT calculations of CH_4 dissociation over Co/MnO catalyst.

To understand the intrinsic catalytic property of our catalyst, the dissociation behavior of CH_4 was representatively calculated. Each dissociation step of CH_4 over the surface of Co/MnO was simulated. Based on the DFT calculation, the cleavage of the first C-H bond on Co/MnO is exothermic by -0.81 eV, indicating that the first step dehydrogenation in CH_4 is very efficient. The exothermic energy is even larger than the reported for Ni/CeO_2 based catalyst[56], indicating excellent activity of Co/MnO as catalyst. Following the dehydrogenation, the resulting CH_3 species bonded atop to the surface of the Co atom and the H atom moved to the neighboring Co atom (Fig. 7a). Different from the dissociation of the first C-H bond, the next dehydrogenation step from CH_3 to CH_2 is strongly thermodynamically unfavorable due to the high Gibbs free energy needed by the cleavage reaction. As calculated in Fig. 7b, the Gibbs free energy in this step is as high as 1.19 eV. The high Gibbs free energy leads to significantly disfavorable dissociation of CH_3 on Co/MnO catalyst, in line with the dissociation behavior of CH_3 on Ni-based catalysts (e.g., Ni/CeO_2)[61]. As reported in the literature[61], compared with the highly endothermic dehydrogenation step from CH_3 to CH_2, oxidation of CH_3 to CH_3O, for example on a Ni/CeO_2 catalyst, in the dry reforming of

methane is exothermic, which would be a preferable route in this step. Additionally, the DFT calculations were run at 0 K, while the catalytic reactions were performed at temperatures of higher than 1000 K, which has a significant effect on the Gibbs enthalpy of exothermal and endothermal reactions. Under elevated temperatures, exothermal reactions get less favorable while endothermal reactions get more favorable. Moreover, oxidation of CH_3 to CH_3O could lead to the formation of large amounts of CO and failure of carbon deposition, which is paradoxical to the results in this work. Hence, direct dehydrogenation from CH_3 to CH_2 should be the exclusive route in this work. With the further progressing of the dehydrogenation process, the energy needed by the cleavage of the C-H bond increased. As shown in Fig. 7b, the energy needed by the dissociation reaction from CH_2 and CH to CH and C, respectively, was as high as 1.47 eV and 2.41 eV due to the thermodynamic stability of CH_2 and CH. In the last two steps of the dehydrogenation process, the formation of the H-H bond and H_2 desorption is exothermic by -2.99 eV and -0.27 eV, which is thermodynamic favorable. By comparison with the DFT calculation results in the literature[61], the Co/MnO catalyst designed in this work is an active catalyst in the catalytic conversion of CH_4.

3.4 Electrochemical performance of the resulting CNCs

To explore the potential application of CNCs as LIB anode, the resulting CNCs after the catalytic reaction were selectively tested. Fig. 8a presents the extended cycling performance as an anode for lithium-ion batteries of the CNCs catalyzed with Cat.-$CoMn_2$ at a temperature of 800 ^oC at the pre-catalyst to plastic weight ratio of 1:20. The initial discharge capacity of the CNCs can reach up to 770.1 $mAh \cdot g^{-1}$ and maintain a reversible capacity of 522.4 $mAh \cdot g^{-1}$ after 100 cycles, which outperforms the commercial carbon-based anodes such as graphite used for LIB [64-66]. Besides, the coulombic efficiency of the prepared anode has always been kept above 95% after the first 6 cycles. The remarkable cycling performance is attributed to the unique network structure and elemental composition of the CNCs, making them a potential candidate for the high-performance anodes in

lithium-ion batteries. The cyclic voltammograms tests of the CNCs are shown in Fig. 8b. During the initial discharge process, the first anodic peak appeared at ~0.62 V corresponds to the conversion of Co^{2+} to metallic Co and Mn^{2+} to metallic Mn[67,68]. While the second anodic peak at ~0.19 V represents the formation of the solid-electrolyte interface (SEI) films on the surface of the materials[67]. Besides, the third anodic peak close to 0 is related to the insertion of lithium ions into carbon nanotubes[11,69]. During the charging process, there are three oxidation peaks. The first one at ~0.26 V is attributed to the delithiation of the carbon nanotube[11,69], whereas the second one at ~1.27 V and the third one at ~2 V are related to the oxidation of Co and Mn to Co^{2+} and Mn^{2+}, respectively[67,68]. An obviously shifted anodic peak at ~0.5 V from the second cycle on is discussed to be attributed to the electrode polarization[68, 70-72]. However, all CV curves mostly overlap from the third cycle indicating that the electrode structure and reversible electrochemical reaction tend to be stable[67]. Therefore, the CNCs exhibit excellent extended cycling performance as mentioned before.

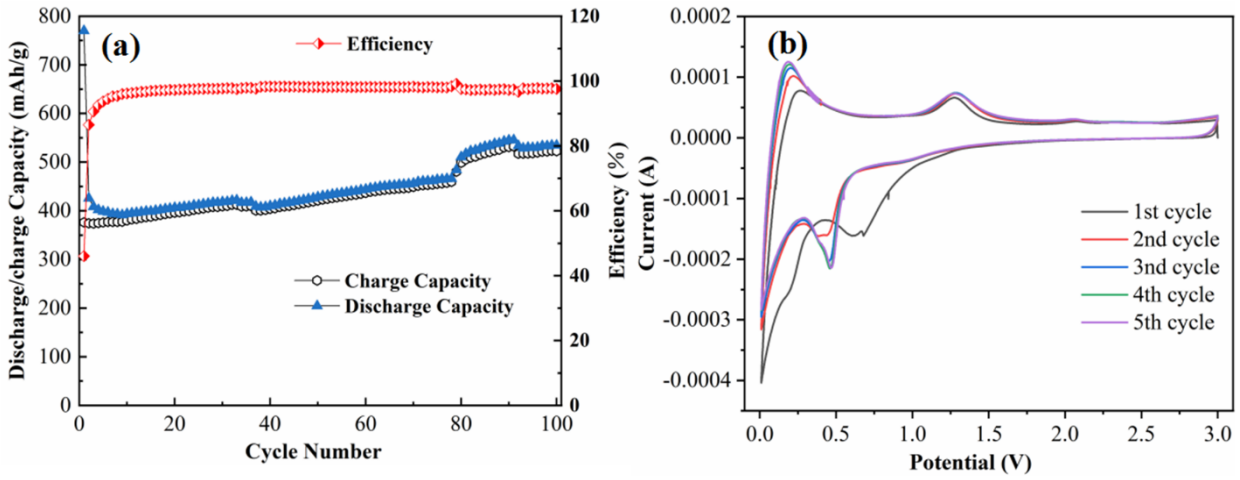

Fig. 8 (a) Charge-discharge voltage profiles at 0.1 $A \cdot g^{-1}$ for 100 cycles and (b) cycling performance at a scan rate of 0.2 mV/s of CNCs catalyzed by Cat.-Co_1Mn_2 at 800 ˚C at a pre-catalyst to plastic weight ratio of 1:20.

4. **Conclusion**

In this work, 3D porous $Co_xMn_{3-x}O_4$ spinel smart pre-catalysts that can self-convert into the targeted active site-rich Co/MnO catalysts were successfully developed via a multiscale designed strategy and employed for the conversion of waste plastic to CNCs and H_2. The targeted Co/MnO catalysts were formed in situ by reduction of $Co_xMn_{3-x}O_4$ spinels via the hydrocarbons decomposed from the waste plastic. Due to the excellent catalytic activity towards hydrocarbon dissociation and active-site rich structure, the smart pre-catalysts derived Co/MnO catalysts exhibited excellent catalytic performance in relation to carbon and H_2 yield. The catalytic performance of Co/MnO catalysts varied with the change of catalytic reaction temperature and composition. At a temperature of 800 ^oC, the Cat-Co_2Mn catalyst exhibited the best catalytic performance among all prepared catalysts (e.g., Cat.-Co_1Mn_2, Cat.-$Co_{1.5}Mn_{1.5}$, Cat.-Co_2Mn_1, and Cat.-$Co_{2.5}Mn_{0.5}$,). When the weight ratio of pre-catalyst (Co_2MnO_4) to plastic weight ratio is 1:14, the carbon and H_2 yield can reach as high as 41 wt.% and 36 $mmol \cdot g^{-1}$, while the specific carbon and H_2 yield reached unprecedented high values of 7.48 $g^{-1}_{pla.}$ and 634 $mmol \cdot g^{-1}_{pla.} \cdot g^{-1}_{cat.}$, which is more than one order of magnitude higher than reported in literature. DFT calculations indicated that the Co/MnO catalyst exhibited excellent activity in CH_4 dissociation. The resulting CNCs exhibit excellent discharge capability and extended cycling performance when they were used as a LIB anode. This work developed an innovative route for the design of advanced catalysts for the conversion of plastic waste via the pyrolysis-catalysis method.

Acknowledgements

M. W. and A. W. highly acknowledge the funding by the German Federal Ministry of Education and Research (BMBF) within the NexPlas project (project number: 03SF0618B). Y. S. Z is grateful

for financial supports provided by the Royal Society of Chemistry Enablement Grant (E21-5819318767) and Royal Society of Chemistry Mobility Grant (M19-2899).

Author contributions

X.L. and D.X. : Investigation, Methodology, Validation, Writing-original draft. D.H., M. M., F.Q., Z.Z., and A.R. : Investigation. M.W. and W.X.: Investigation, Methodology, Validation, Writing-original draft. Y.Z., L.M.L., D.J.L.B., J.P.H., and R.R.: Writing-review & editing. A.W.: Funding acquisition, Conceptualization, Supervision, Writing-review & editing.

Declaration of interests

The authors declare no conflict of interests.

Reference

1. X. Zeng, M. Li, D. Abd, W. El-Hady Alshitari, A.S. Al-Bogami, J. Lu, K. Amine, Commercialization of lithium battery technologies for electric vehicles. Adv. Energy Mater. (2019) 9 1900161.

2. D. Liu, Z. Shadike, R. Lin, K. Qian, H. Li, K. Li, S. Wang, Q. Yu, M. Liu, S. Ganapathy, X. Qin, Review of recent development of in situ/operando characterization techniques for lithium battery research, Adv. Mater. 31 (2019) 1806620.

3. F. Dawood, M. Anda, G.M. Shafiullah, Hydrogen production for energy: An overview. Int. J. Hydrog. Energy. 45 (2020) 3847-69.

4. G. Chen, X. Tu, G. Homm, A. Weidenkaff, Plasma pyrolysis for a sustainable hydrogen economy. Nat. Rev. Mater. (2022) 1-2.

5. C. Acar, I. Dincer, Review and evaluation of hydrogen production options for better environment. J. Clean. Prod. 218 (2019) 835-49.

6. N. Akhlaghi, G. Najafpour-Darzi, A comprehensive review on biological hydrogen production. Int. J. Hydrog. Energy. 45 (2020) 22492-512.

7. L. Lu, X. Han, J. Li, J. Hua, M. Ouyang, A review on the key issues for lithium-ion battery management in electric vehicles. J. Power Sources. 226 (2013) 272-88.

8. A. Barré, B. Deguilhem, S. Grolleau, M. Gérard, F. Suard, D. Riu, A review on lithium-ion battery ageing mechanisms and estimations for automotive applications. J. Power Sources. 241 (2013) 680-89.

9. W. Zhang, H. Jin, G. Chen, J. Zhang, Hierarchical 3D N-CNT/Sb_2MoO_6 for dendrite-free lithium metal battery. Chem. Eng. J. 420 (2021) 129614.

10. W. Liu, Y. Fu, Y. Li, S. Chen, Y. Song, L. Wang, Three-dimensional carbon foam surrounded by carbon nanotubes and Co-Co_3O_4 nanoparticles for stable lithium-ion batteries. Compos. B. Eng. 163 (2019) 464-70.

11. Y. Ge, Z. Chen, S. Ye, Z. Zhu, Y. Tu, X. Yang, A spheres-in-tube carbonaceous nanostructure for high-capacity and high-rate lithium–sulfur batteries. J. Mater. Chem. A 6 (2018) 14885-14893.

12. S. Goriparti, U. Gulzar, E. Miele, F. Palazon, A. Scarpellini, S. Marras, C. Capiglia, Facile synthesis of Ge–MWCNT nanocomposite electrodes for high capacity lithium ion batteries. J. Mater. Chem. A 5 (2017) 19721-19728.

13. Y. Zhang, H. Zhu, D. Yao, P. T. Williams, C. Wu, D. Xu, D. Brett, Thermo-chemical conversion of carbonaceous waste for CNT and hydrogen productions: A review. Sustain. Energy Fuels. 5 (2021) 4173-4208.

14. P. T. Williams, Pyrolysis of waste tyres: a review. Waste Manageme. 33 (2013) 1714-1728.

15. P.T. Williams, Hydrogen and carbon nanotubes from pyrolysis-catalysis of waste plastics: A review. Waste Biomass Valorization 12 (2021) 1-28.

16. D. Yao, H. Yang, Q. Hu, Y. Chen, H. Chen, P. T. Williams, Carbon nanotubes from post-consumer waste plastics: Investigations into catalyst metal and support material characteristics. Appl. Catal. B 280 (2021) 119413.

17. D. Yao, Y. Zhang, P. T. Williams, H. Yang, H. Chen, Co-production of hydrogen and carbon nanotubes from real-world waste plastics: Influence of catalyst composition and operational parameters. Appl. Catal. B 221 (2018) 584-597.

18. A.H. Mady, M.L. Baynosa, D. Tuma, J.J. Shim, Heterogeneous activation of peroxymonosulfate by a novel magnetic 3D γ-MnO_2@ $ZnFe_2O_4$/rGO nanohybrid as a robust catalyst for phenol degradation. Appl. Catal. B 244 (2019) 946-956.

19. Y. Wang, H. Sun, H. M. Ang, M. O. Tadé, S. Wang, 3D-hierarchically structured MnO_2 for catalytic oxidation of phenol solutions by activation of peroxymonosulfate: structure dependence and mechanism. Appl. Catal. B 164 (2015) 159-167.

20. X. Liu, W. Xie, M. Widenmeyer, H. Ding, G. Chen, D. M., De Carolis, K., Lakus-Wollny, L., Molina-Luna, R., Riedel, A. Weidenkaff, Upcycling Waste Plastics into Multi-Walled Carbon Nanotube Composites via $NiCo_2O_4$ Catalytic Pyrolysis. Catalyst 11 (2021) 1353.

21. L. Kong, X. Yin, X. Yuan, Y. Zhang, X. Liu, L. Cheng, L. Zhang, Electromagnetic wave absorption properties of graphene modified with carbon nanotube/poly (dimethyl siloxane) composites. Carbon 73 (2014) 185-193.

22. L. Kong, X. Yin, M. Han, X. Yuan, Z. Hou, F. Ye, L. Zhang, L. Cheng Z. Xu, J. Huang, Macroscopic bioinspired graphene sponge modified with in-situ grown carbon nanowires and its electromagnetic properties. Carbon 111 (2017) 94-102.

23. L. Huang, B. White, M. Y. Sfeir, M. Huang, H. X. Huang, S. Wind, J. Hone, S. O'Brien, Cobalt ultrathin film catalyzed ethanol chemical vapor deposition of single-walled carbon nanotubes. J. Phys. Chem. B 110 (2006) 11103-11109.

24. H. R. Byon, H. S. Lim, H.J. Song, H.C. Choi, A synthesis of high purity single-walled carbon nanotubes from small diameters of cobalt nanoparticles by using oxygen-assisted chemical vapor deposition process. B. Korean Chem. Soc. 28 (2007) 2056-2060.

25. X. Jie, W. Li, D. Slocombe, Y. Gao, I. Banerjee, S. Gonzalez-Cortes, B. Yao, H. AlMegren, S. Alshihri, J. Dilworth, J. Thomas, Microwave-initiated catalytic deconstruction of plastic waste into hydrogen and high-value carbons. Nat. Catal. 3 (2020) 902-912.

26. M. A. Nahil, C. Wu, P. T. Williams, Influence of metal addition to Ni-based catalysts for the co-production of carbon nanotubes and hydrogen from the thermal processing of waste polypropylene. Fuel Process. Technol. 130 (2015) 46-53.

27. S. He, Y. Xu, Y. Zhang, S. Bell, C. Wu, Waste plastics recycling for producing high-value carbon nanotubes: Investigation of the influence of Manganese content in Fe-based catalysts. J. Hazard. Mater. 402 (2021) 123726.

28. Q. Zhao, Z. Yan, C. Chen, J. Chen, Spinels: controlled preparation, oxygen reduction/evolution reaction application, and beyond. Chem. Rev. 117 (2017) 10121-10211.

29. M. G. Brik, A. Suchocki, A. Kaminska, Lattice parameters and stability of the spinel compounds in relation to the ionic radii and electronegativities of constituting chemical elements. Inorg. Chem. 53 (2014) 5088-5099.

30. Y. Liang, Y. Li, H. Wang, J. Zhou, J. Wang, T. Regier, H. Dai, Co_3O_4 nanocrystals on graphene as a synergistic catalyst for oxygen reduction reaction. Nat. Mater. 10 (2011) 780-786.

31. J. Kaczmarczyk, F. Zasada, J. Janas, P. Indyka, W. Piskorz, A. Kotarba, Z. Sojka, Thermodynamic stability, redox properties, and reactivity of Mn_3O_4, Fe_3O_4, and Co_3O_4 model catalysts for N_2O decomposition: resolving the origins of steady turnover. ACS Catal. 6 (2016) 1235-1246.

32. Y. Cho, S. Lee, Y. Lee, T. Hong, J. Cho, Spinel-layered core-shell cathode materials for Li-ion batteries. Adv. Energy Mater. 1 (2011) 821-828.

33. F. Cheng, J. Shen, B. Peng, Y. Pan, Z. Tao, J. Chen, Rapid room-temperature synthesis of nanocrystalline spinels as oxygen reduction and evolution electrocatalysts. Nat. Chem. 3 (2011) 79-84.

34. D. Xu, Y. Xiong, J. Ye, Y. Su, Q. Dong, S. Zhang, Performances of syngas production and deposited coke regulation during co-gasification of biomass and plastic wastes over Ni/γ-Al_2O_3 catalyst: Role of biomass to plastic ratio in feedstock. Chem. Eng. J. 392 (2020) 123728.

35. Fairley, N. Fernandez, V. Richard-Plouet, M. Guillot-Deudon, C. Walton, J. Smith, E. Flahaut, D. Greiner, M. Biesinger, M. Tougaard, S. Morgan, D. Systematic and collaborative approach to problem solving using X-ray photoelectron spectroscopy. Appl. Surf. Sci. 5 (2021) 100112.

36. G. Kresse, J. Furthmüller, Efficiency of ab-initio total energy calculations for metals and semiconductors using a plane-wave basis set. Comp. Mater. Sci. 6 (1996) 15-50.

37. G. Kresse, J. Hafner, Ab-Initio Molecular-Dynamics Simulation of the Liquid-Metal Amorphous Semiconductor Transition in Germanium. Phys. Rev. B 49 (1994) 14251-14269.

38. G. Kresse, J. Hafner, Ab initio molecular dynamics for liquid metals. Phys. Rev. B 47 (1993) 558-561.

39. J.P. Perdew, K. Burke, M. Ernzerhof, Generalized Gradient Approximation Made Simple. Phys. Rev. Lett. 77 (1996) 3865-3868.

40. E. Uchaker, N. Zhou, Y Li, G. Cao, Polyol-mediated solvothermal synthesis and electrochemical performance of nanostructured V_2O_5 hollow microspheres. J. Phys. Chem. C 117 (2013) 1621-1626.

41. S. Chen, P. Bao, X. Huang, B. Sun, G. Wang, Hierarchical 3D mesoporous silicon@ graphene nanoarchitectures for lithium ion batteries with superior performance. Nano Res. 7 (2014) 85-94.

42. J. Habjanic, M. Juric, J. Popovic, K. Molcanov, D. Pajic, A 3D oxalate-based network as a precursor for the $CoMn_2O_4$ spinel: synthesis and structural and magnetic studies. Inorg. Chem. 53 (2014) 9633-9643.

43. C. Dong, Z. Qu, Y. Qin, Q. Fu, H. Sun, X. Duan, Revealing the highly catalytic performance of spinel CoMn2O4 for toluene oxidation: involvement and replenishment of oxygen species using in situ designed-TP techniques. ACS Catal. 9 (2019) 6698-6710.

44. F. Chen, Z. Wang, S. Huo, S. Ji, H. Wang, P. Zhou, Cubic $CoMn_2O_4$ particles directly grown on Ni foam as binder-free electrode for asymmetric supercapacitors. Mater. Lett. 237 (2019) 209-212.

45. R.D. Shannon Revised effective ionic radii and systematic studies of interatomic distances in halides and chalcogenides. Acta crystallographica section A: crystal physics, diffraction, theoretical and general crystallography. 32 (1976) 751-67.

46. S. Wang, Y. Hou, X. Wang, Development of a stable $MnCo_2O_4$ cocatalyst for photocatalytic CO_2 reduction with visible light. ACS Appl. Mater. Inter. 7 (2015) 4327-4335.

47. J.H. Van Vleck, The dirac vector model in complex spectra. Phys. Rev. 45 (1934) 405.

48. V.R. Galakhov, S. Uhlenbrock, S. Bartkowski, A.V. Postnikov, M. Neumann, L.D. Finkelstein, E.Z. Kurmaev, A.A. Samokhvalov, L.I. Leonyuk, X-ray photoelectron 3s spectra of transition metal oxides. (1999)

49. G. Van der Laan, C. Westra, C. Haas, G.A. Sawatzky, Satellite structure in photoelectron and Auger spectra of copper dihalides. Phys. Rev. B 23 (1981) 4369.

50. Galakhov, V.R., Karelina, V.V., Kellerman, D.G., Gorshkov, V.S., Ovechkina, N.A., and Neumann, M. (2002). Electronic structure, x-ray spectra, and magnetic properties of the $LiCoO_{2-\delta}$ and Na_xCoO_2 nonstoichiometric oxides. Phys. Solid State 44, 266-273.

51. L. Dahéron, R. Dedryvère, H. Martinez, M. Ménétrier, C. Denage, C. Delmas, D.Gonbeau, Electron transfer mechanisms upon lithium deintercalation from $LiCoO_2$ to CoO_2 investigated by XPS. Chem. Mater. 20 (2008) 583-590.

52. Z.X. Shen, J.W. Allen, P.A.P. Lindberg, D.S. Dessau, B.O. Wells, A. Borg, W. Ellis, J.S. Kang, S.J. Oh, I. Lindau, W.E. Spicer, Photoemission study of CoO. Phys. Rev. B 42 (1990) 1817.

53. D. Yao, C. Wu, H. Yang, Y. Zhang, M.A.Nahil, Y. Chen, P.T.Williams, H. Chen, Co-production of hydrogen and carbon nanotubes from catalytic pyrolysis of waste plastics on Ni-Fe bimetallic catalyst. Energy Convers. Manage. 148 (2017) 692-700.

54. C. Wu, P.T. Williams Hydrogen production by steam gasification of polypropylene with various nickel catalysts. Appl. Catal. B. 87 (2009) 152-61.

55. R.X. Yang, K.H. Chuang, M.Y. Wey, Effects of nickel species on Ni/Al_2O_3 catalysts in carbon nanotube and hydrogen production by waste plastic gasification: bench-and pilot-scale tests. Energy Fuels. 29 (2015) 8178-87.

56. D. Yao C.H Wang Pyrolysis and in-line catalytic decomposition of polypropylene to carbon nanomaterials and hydrogen over Fe-and Ni-based catalysts. Appl. Energy 265 (2020) 114819.

57. D.Yao, H. Li, Y. Dai, C.H. Wang, Impact of temperature on the activity of Fe-Ni catalysts for pyrolysis and decomposition processing of plastic waste. Chem. Eng. J. 408 (2021) 127268.

58. G. Du, S. Feng, J. Zhao, C. Song, S. Bai, Z. Zhu, Particle− wire− tube mechanism for carbon nanotube evolution. J. Am. Chem. Soc. 128 (2006) 15405-15414.

59. C.P. Deck, K. Vecchio, Growth mechanism of vapor phase CVD-grown multi-walled carbon nanotubes. Carbon 43 (2005) 2608-2617.

60. Y. Tang, Y. Wei, Z. Wang, S. Zhang, Y. Li, L. Nguyen, Y. Li, Y. Zhou, W. Shen, F.F. Tao, P. Hu, Synergy of single-atom Ni1 and Ru1 sites on CeO_2 for dry reforming of CH_4. J. Am. Chem. Soc. 141 (2019) 7283-93.

61. M. Akri, S. Zhao, X. Li, K. Zang, A.F. Lee, M.A. Isaacs, W. Xi, Y. Gangarajula, J. Luo, Y. Ren, Y.T. Cui, Atomically dispersed nickel as coke-resistant active sites for methane dry reforming. Nat. Commun. 10 (2019) 1-10.

62. Z. Zuo, S. Liu, Z. Wang, C. Liu, W. Huang, J. Huang, P. Liu, Dry reforming of methane on single-site Ni/MgO catalysts: importance of site confinement. ACS Catal. 8 (2018) 9821-35.

63. M. Yusfi, R. Jonuarti, T.D. Wungu, M.M. Munir, The adsorption of C_2H_2, C_2H_4, and C_2H_6 on single Fe atom doped SWCNT: a density functional theory study. Int. J. Nanoelectron. Mater. 13 (2020) 113-20.

64. M. Armand, J.M. Tarascon, Issues and challenges facing rechargeable lithium batteries. Nature 414 (2001) 359-67.

65. E. Frackowiak, F. Beguin, Electrochemical storage of energy in carbon nanotubes and nanostructured carbons. Carbon 40 (2002) 1775-87.

66. S. Goriparti, E. Miele, F. De Angelis, E. Di Fabrizio, R.P. Zaccaria, C. Capiglia, Review on recent progress of nanostructured anode materials for Li-ion batteries. J. Power Sources 257 (2014) 421-43.

67. L. Zhou. D. Zhao, X.W. Lou, Double-shelled $CoMn_2O_4$ hollow microcubes as high-capacity anodes for lithium-ion batteries. Adv. Mater. 24 (2012) 745-8.

68. X. Pan, J. Ma, R. Yuan, X. Yang Layered double hydroxides for preparing $CoMn_2O_4$ nanoparticles as anodes of lithium ion batteries. Mater. Chem. Phys. 194 (2017) 137-41.

69. B.J. Landi, M.J. Ganter, C.D. Cress, R.A. DiLeo, R.P. Raffaelle, Carbon nanotubes for lithium ion batteries. Energy Environ. Sci. 2 (2009) 638-54.

70. W. Dang, C. Feng, P. Deng, L. Xiao, Z. Ban., X. Tang, Y. Zhang, Optimized pseudocapacitance of $CoMn_2O_4$@MoO_3 nano–microspheres for advanced lithium storage properties. J. Mater. Sci. 56 (2021) 649-63.

71. J.S. Do, C,H. Weng, Electrochemical and charge/discharge properties of the synthesized cobalt oxide as anode material in Li-ion batteries. J. Power Sources 159 (2006) 323-7.

72. C. Qiu, G. He, W. Shi, M. Zou, C. Liu, The polarization characteristics of lithium-ion batteries under cyclic charge and discharge. J. Solid State Electr. 23 (2019) 1887-902.